# VELOCITY MODEL BUILDING: A COMPARISON BETWEEN PRESTACK STEREOTOMOGRAPHY AND NIP-WAVE TOMOGRAPHY

*K. Meier, S. Dümmong, D. Gajewski, and C. Hübscher*

**email:** *kristina.meier@zmaw.de*

**keywords:** *Velocity model building, tomography*

**ABSTRACT**

*Velocity model determination during seismic data processing is crucial for any kind of depth imaging. Tomography procedures are often used to determine these models. In this article we compare two different approaches of grid tomography: prestack stereotomography (PST) and NIP-wave tomography (NIPT). Whereas NIPT is based on CRS stack attributes and thus on the underlying hyperbolic second-order traveltime approximation PST describes traveltimes by local slopes (i.e. linearly) in the prestack data domain. To analyse the impact of the different traveltime approximations on velocity model building we have applied both techniques to a synthetic and a real marine dataset. The obtained velocity models reveal that the reconstruction of high velocity contrasts is limited due to the smooth description of the velocity distribution. The lateral resolution of velocities in PST appears to be slightly better than in NIPT which might be related to the local approximation of traveltimes. Other differences are mainly caused by picks in PST which correspond to refracted waves with linear moveout. They restrain correct velocity estimation since only reflected events should be considered in the PST model building process, whereas NIPT is not affected since refracted events can not be matched by a hyperbolic traveltime curve. Careful pre-processing of the data therefore will improve the PST model building as well as the depth imaging in both cases.*

## INTRODUCTION

For the transformation of the recorded seismic data to the desired depth section, a correct migration velocity model is always required. Different approaches for velocity model estimation have been proposed in the past. They can be mainly divided into two groups: migration-based velocity analysis methods and tomographic methods. Two of these methods belonging to the second group are prestack stereotomography by Billette and Lambaré (1998) and NIP-wave tomography by Duveneck (2004).

In stereotomography, reflection traveltimes are approximated by local slopes which are directly linked to the horizontal component of the slowness vector. These slopes, their related traveltimes and spatial positions at the surface are used for the estimation of a smooth velocity model. They are obtained in the prestack data domain by automated picking. Since only locally coherent events are considered no assumptions on the lateral heterogeneity of the velocity distribution nor the continuity of any interfaces are made.

NIP-wave tomography depends on information resulting from the CRS stack e.g.(Mann, 2002) and is consequently based on the hyperbolic second-order traveltime approximation underlying the CRS stacked sections. The parameters used for velocity model estimation are the wavefront curvatures and the angle of emergence picked from the CRS stack attribute sections. Picking of these attributes is facilitated due to the high signal to noise ratio in the post stack domain. In NIP-wave tomography, the extracted wavefield parameters do not need to belong to a consistent event, the only demand is that they are reliably estimated. Both methods are based on a grid tomographic approach, therefore leading to a smooth velocity model.

Unlike conventional horizon-based schemes no interpretive input is necessary; however, the resolution of structural boundaries is limited. In this article, we compare both methods to analyse the impact of their differences in input data determination and traveltime approximation on velocity model building.
In the following section, the theory of both tomographic methods is described briefly and differences are pointed out. Then, the methods are applied to two datasets: first to a synthetic dataset to demonstrate general differences between both schemes and second to a real marine dataset from the Eastern Mediterranean. In the latter, a large salt body is imaged with an overburden of young sediments. Both algorithms have to deal with complex geological structures and high velocity contrasts.

## THEORY

### Stereotomography

Prestack stereotomography was proposed, developed and applied by Billette and Lambaré (1998). It belongs to the family of slope tomographic methods and is based on the concept of locally coherent events. These are seismic events which have to be tracked only over a limited number of traces around a central trace. In stereotomography the attributes of these events are used for the estimation of a smooth velocity macro-model.

Seismic events are characterised by the position of their central trace, i.e its associated source and receiver position $(S, R)$, by their central two-way traveltime $T_{SR}$ and by their local slopes, i.e. the tangents on the traveltime curves around a central trace in a common-shot and a common-receiver-gather $(p_R, p_S)$. Since only locally coherent events are considered each set of parameters $(S, R, p_S, p_R, T_{SR})$ provides information on the velocity model independently of all other events. Consequently, no assumptions on interfaces nor on the velocity distribution are necessary.
As in all slope tomographic methods, in addition to traveltime information the slopes constrain the velocity model as they are directly linked to the horizontal component of the slowness vector. Each event corresponds to a pair of ray segments from a reflection/diffraction point $X$ in the subsurface velocity model to either the source or the receiver. Each ray segment is completely defined by its starting and ending point, its angle of emergence or incidence $(\theta_S, \theta_R)$ and the associated one-way traveltime $(T_S, T_R)$, to the source and receiver respectively. In the case of a correct velocity model both segments will satisfy the following boundary conditions:

- they must join each other at the reflection/diffraction point in depth
- they must explain the positions, slopes and two-way traveltimes of the events at the surface

If the velocity model is incorrect, these conditions cannot be satisfied by both ray segments simultaneously. This means that at least one of the boundary conditions has to be 'relaxed' (become variable). This principle is used by stereotomography: the difference between the parameters describing the relaxed boundary condition and the ideal situation (i.e. a pair of ray segments in the correct model) is used to constrain the velocity model. Based on this, an inverse problem in which the model space is described by the velocity field and a group of ray segment pairs is constructed.

In practice, the boundary condition at the surface is relaxed and a cost function containing the misfits in source and receiver positions, associated slopes and traveltimes is evaluated. The data measured at the surface are fitted in a least square sense to data modelled by ray-tracing in a smooth velocity model described by cardinal cubic B-splines. Thus, the model space in stereotomography is composed of a discrete description of the velocity field denoted as B-spline coefficients $v_{ij}$, a group of reflecting/diffracting points, two angles of emergence and two one-way traveltimes. These parameters are updated by a joint inversion until they explain each data point $(S, R, p_S, p_R, T_{SR})_n$ within prescribed error margins. For inversion a conjugate gradient method called LSQR (Paige and Saunders, 1982) is used.

### NIP-wave tomography

NIP-wave tomography uses the concept of 'having a NIP-wavefront shrinked back to its hypothetical source' (Hubral and Krey, 1980) which is related to the principle of depth focussing analysis in the de-

termination of migration velocities (MacKay and Abma, 1992).
The NIP-wave is a hypothetical wave which starts at the Normal Incidence Point (NIP) of a reflector in depth and arrives with a certain angle at the corresponding Zero Offset point at the surface. The NIP is associated with the Common Reflection Point (CRP) for the same Zero offset position. Thus the NIP-waves are linked to a certain point in the subsurface for a given velocity model. All NIP-waves focus at zero time if the velocity model is consistent with the data.
The CRS stack is a multiparameter stacking method based on a hyperbolic second-order traveltime approximation. The input data for NIP-wave tomography are obtained from the CRS stack and the accompanying attribute sections. These attributes are also referred to as CRS parameters. They are used to estimate the smooth velocity distribution.
Since the NIP-wave tomography inversion scheme is based on a second-order approximation of the traveltimes the algorithm is limited to regions with moderate lateral velocity variations. However, the advantage of estimating all parameters in the CRS stacked sections with a high signal to noise ratio significantly simplifies the picking of the attributes. Therefore, NIP-wave tomography is applicable to data with low signal to noise ratio.

The inversion problem for the 2D case can be formulated in the following way: the emerging NIP-wavefront can be characterised by four parameters, the traveltime of the normal ray $\tau = t_0/2$, the corresponding coordinate at the surface $x$, the horizontal slowness component $p$ and the second spatial derivative of the traveltime $M_{NIP}$. Thus an emerging NIP-wave can be characterised by the data point $(\tau, M_{NIP}, p, x)$. The true subsurface locations $(X, Z)$ and the local dips $\alpha$, defining the normal ray direction are initially unknown. They are determined during the inversion process along with the smooth velocity distribution which is described by two dimensional B-splines. The subsurface model description is given by $(X, Z, \alpha, v_{ij})$, where $v_{ij}$ denotes the B-spline coefficients. The velocity distribution is determined in the following way: Dynamic ray tracing is performed starting at the CRPs in depth. By minimising in a least square sense the misfit between the modelled data and the data points extracted from the CRS stack at the surface, the algorithm is able to find the velocity model that fits the data best. The inversion problem is solved by a conjugate gradient scheme (LSQR) (Paige and Saunders, 1982).

**Differences**

There are two major differences between prestack stereotomography and NIP-wave tomography. First, the input data for the tomographic inversions are determined in two different data domains. In prestack stereotomography information is obtained in the prestack data domain by an automated picking procedure based on local slant stack panels. In contrast, in NIP-wave tomography the input data is picked in the poststack data domain using the results of the CRS stack. Here events are more easily identified due to the high signal to noise ratio.
The second major difference is the representation of the traveltimes. In NIP-wave tomography, the entire traveltime curve is approximated, hence it is a global approach. Seismic events are assumed to have a hyperbolic shape, otherwise they can not be picked nor inverted correctly. This reduces the applicability of the method for complex lateral inhomogeneous media. In prestack stereotomography traveltimes are described by local slopes of locally coherent events, thus only a part of the traveltime curve described by its tangent (local approach).
Both differences are directly related to the formulation of the tomographic problem. In prestack stereotomography local slopes, their corresponding twoway-traveltime and spatial positions are used as input. In NIP-wave tomography the zero-offset traveltime, the spatial position, the horizontal slowness component and the second-order spatial derivatives of the traveltime are used.
In both methods, the input data are fitted in a least square sense to modelled data calculated by dynamic ray-tracing using an conjugate gradient inversion scheme and a smooth velocity model is obtained.

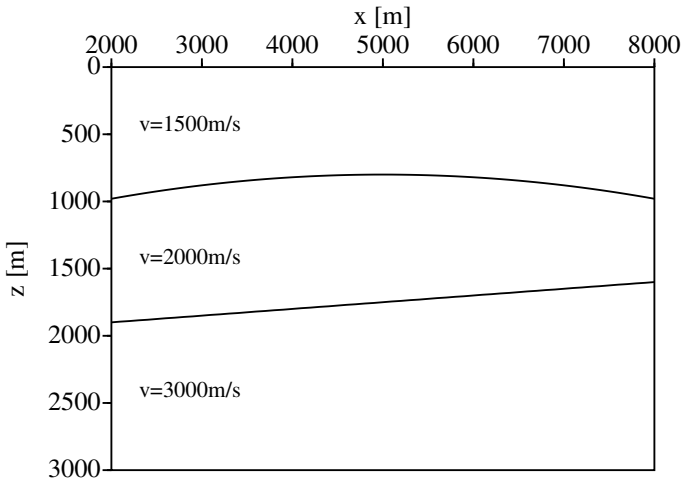


**Figure 1:** The velocity model used for the modelling of the synthetic dataset.

## DATA EXAMPLES

### Synthetic data example

In this part we compare the inversion results of both methods under controlled conditions using a synthetic dataset. The underlying model in Fig. 2 consists of one curved and one inclined interface and the velocities vary from 1500 m/s to 3000 m/s. Seismograms were modelled by a ray tracing method and a zerophase wavelet was used. In total the dataset consists of 700 CMP locations with a spacing of 20 m. The maximum offset is 2000 m. Gaussian noise was added to the seismograms, a signal to noise ratio of 2 was used.

**Stereotomography results** For the estimation of input data for the stereotomographic scheme an automatic picking tool based on local slant stack panels (Billette et al., 2003) was used scanning all shot- and receiver-gathers for locally coherent events. Semblance was estimated every 20 m, i.e. at every shot and receiver position. 10 traces with a spread of 200 m were used for local slant stack calculation. A subsequent quality control as described in Billette et al. (2003) was applied to the picks, where only events with a semblance greater than 0.65 were accepted as input for the tomographic inversion.

Prior to the inversion an initial velocity model was created on a B-spline grid with a node spacing of 1 km laterally and 0.5 km vertically. A starting velocity-depth function of $V(z) = 1500$ m/s $+ 0.5$ s$^{-1} \times z$ was assumed. The error margins for each data point were set to 1 m for the positions, 4 ms for the traveltime and 0.01 ms/m for the slopes, as commonly used. Based on this input and the selected picks the inversion procedure was started. It consisted of 10 inversion steps, a subsequent elimination of outliers in normalised square misfits as proposed by Lambaré et al. (2004a) and 15 additional inversion steps. The best velocity model was obtained after 9 iterations following the outlier removal, where the cost function reaches the prescribed minimum.

The final model and the corresponding migrated image are shown in Fig. 2. The positions of the interfaces were recovered. The analysis of the common image gathers not shown here, also reveals that the gathers are well flattened. The velocity model was estimated correctly by stereotomography.

**NIP-wave tomography results** For NIP-wave tomography the necessary input information was created by means of the CRS stack. To facilitate the subsequent picking in the CRS attribute sections event consistent parameter smoothing (Hertweck et al., 2005) was applied. An automated picking algorithm extracted the input data. During this step events are mainly identified by semblance criteria so that their selection depends on a given semblance threshold. Based on the obtained coherency section of the CRS Stack a minimal semblance of 0.2 proved to be suitable. For the purpose of outlier elimination a quality control

sequence using stacking velocity criteria was applied.

For the NIP-tomographic inversion the same initial velocity model and distribution of B-spline nodes as in stereotomography was used. Assuming that all input parameters were determined with the same error, all parameters were weighted equally during the inversion process. After 10 iterations the inversion was stopped since no further significant decrease of the cost function was observed.

The resulting velocity model and its corresponding migrated image are shown in Fig. 2. As in stereotomography the positions of the interfaces were recovered very well. The examination of the common image gathers not shown here proves a good estimation of the velocity distribution since all gathers are flattened.

**Comparison** Both tomographic approaches estimate a correct migration velocity model. In both cases the positions of the interfaces are completely recovered and all common image gathers show flat events. Nevertheless, the smooth description of the velocity distribution leads to velocity smearing, but both models provide good migration results. In the constraint areas, i.e. the areas where picks (interfaces) are present no major differences can be noted. However, the velocity model found by stereotomography recovers better the dipping character of the second interface in this comparison, but if the node spacing is reduced the same results can be obtained by NIP-wave tomography.

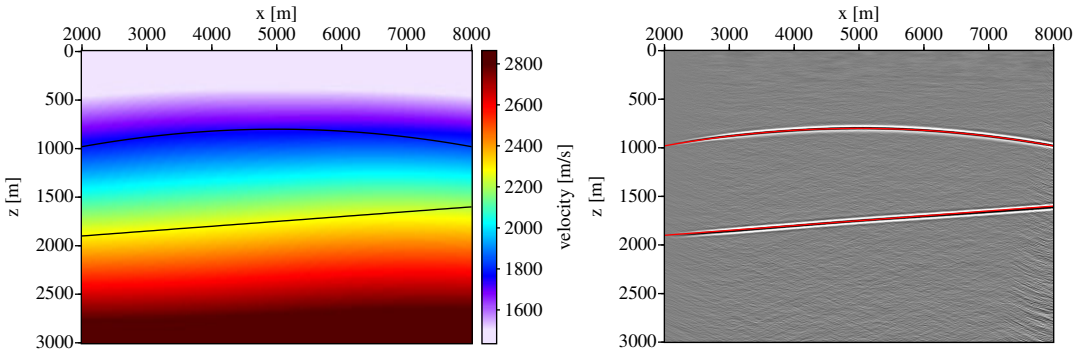


**(a)** Stereotomography result.




**(b)** Corresponding migrated section.

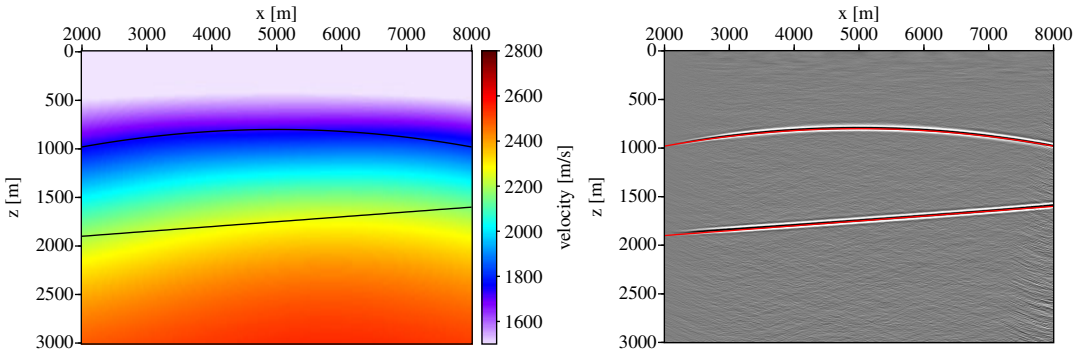


**(c)** Nip tomography result.




**(d)** Corresponding migrated section.

**Figure 2:** Results of stereotomography and NIP-wave tomography from the synthetic dataset. On the left, the obtained velocity model is displayed with the true model boundaries in black. The right figure shows the corresponding migrated section with the true model boundaries in red.

### Real data example

In this section we will demonstrate the application of the two inversion methods to a real marine data example from the Eastern Mediterranean. The acquisition was performed on a straight line with a shot and and receiver spacing of 25 m with maximal offsets of 7325 m. An extract of the dataset of 1000 CMPs was processed.

**Geologic setting** The data example from the central Levantine Basin/eastern Mediterranean covers the so called Messinian Evaporites (ME), the Pliocene-Quaternary overburden and the upper pre-Messinian succession. The ME precipitated during the Messinian Salinity Crisis when the interaction of plate tectonics and and eustatic sea level fall led to the closure of the gateway between the Mediterranean and the Atlantic (Hsü et al., 1980). Recent publications showed a complex seismic stratigraphy of the evaporites in the Levantine Basin (Netzeband et al., 2006b; Bertoni and Cartwright, 2006). The deformation pattern of the intra-evaporitic sequences include folds and thrust faulting, which gives evidence for extensive salt tectonics and shortening, respectively, during the depositional phase. Both the identified evaporitic facies of the individual intra-evaporitic sequences and the driving forces for the syn-depositional shortening remain unclear.

Velocity model calculation and depth-migration in salt bearing basins is a challenging task for several reasons. The vertical velocity contrast between the ME and the overburden is bigger than 2 km/s, since interval-velocities of $4.3 - 4.4$ km/s have been calculated for the evaporites and $1.7 - 2.1$ km/s for the overburden, respectively (Netzeband et al., 2006a). If the ME are folded, strong lateral velocity contrasts occur at their top. Small thickness undulations of the ME cause apparent reflection undulations beneath (velocity pull-ups/-downs), which may be spuriously interpreted as folds or faults. The intra-evaporitic reflections reveal much weaker amplitudes than the top or base of the ME. In the following, the upper boundary between the ME and the overburden at a depth of about 2200 m will be called the M-reflection and the lower one at a depth of about 3500 m the N-reflection.

**Stereotomography results** As in the synthetic case an automated picking procedure in the prestack data domain was used for input data determination. However, in the real data case some additional preprocessing was necessary. It consisted mainly of an inner and outer mute and a $t^2$-gain control in order to focus the picking on the relevant part of the traces. After preprocessing, semblance was estimated every 20 m using 8 traces for local slant stack calculation. Due to strong differences in the energy of events for earlier and later times the data were split in two parts. The upper part contains picks describing the overburden. During a subsequent quality control events with a semblance greater than 0.6 were accepted. In the lower part an additional gain control was applied and the semblance threshold was decreased to 0.2.

To complete the input data for the stereotomographic inversion, an initial velocity model was created on a coarse B-spline grid of 500 m $\times$ 500 m where a preliminary velocity gradient of $V(z) = 1550$ m/s $+ 0.45$ s$^{-1} \times z$ was assumed. Artificial picks describing the water column were added to better constrain the model in this region. Based on these assumptions the inversion was started. First, 15 inversions were performed followed by an elimination of outliers in normalised square misfits. For this purpose the error margins were introduced as 5 m for positions, 4 ms for traveltimes and 0.01 ms/m for the slopes as mentioned above. To resume, another 35 inversions were performed and first results were used for an advanced quality control procedure (Lambaré et al., 2004b). Finally, in order to increase the vertical resolution of the model we refined the node spacing to 125 m vertically and after 11 further iterations velocity model estimation was stopped since no further significant decrease of the cost-function could be observed.

The resulting stereotomographic model is displayed in Fig. 3. The velocity distribution is shown together with dip bars. These bars are characterised by the spatial distribution of the picked reflection/diffraction points as well as by a local dip. The velocity distribution is clearly linked to the structures picked in the model. At about 1700 m depth a smooth increase in velocity indicates the seafloor and in the subsequent part the velocity rises to 2500 m/s corresponding to the overburden of young sediments. At a depth of approximately 2200 m a strong velocity gradient dominates the model. This gradient matches the top of

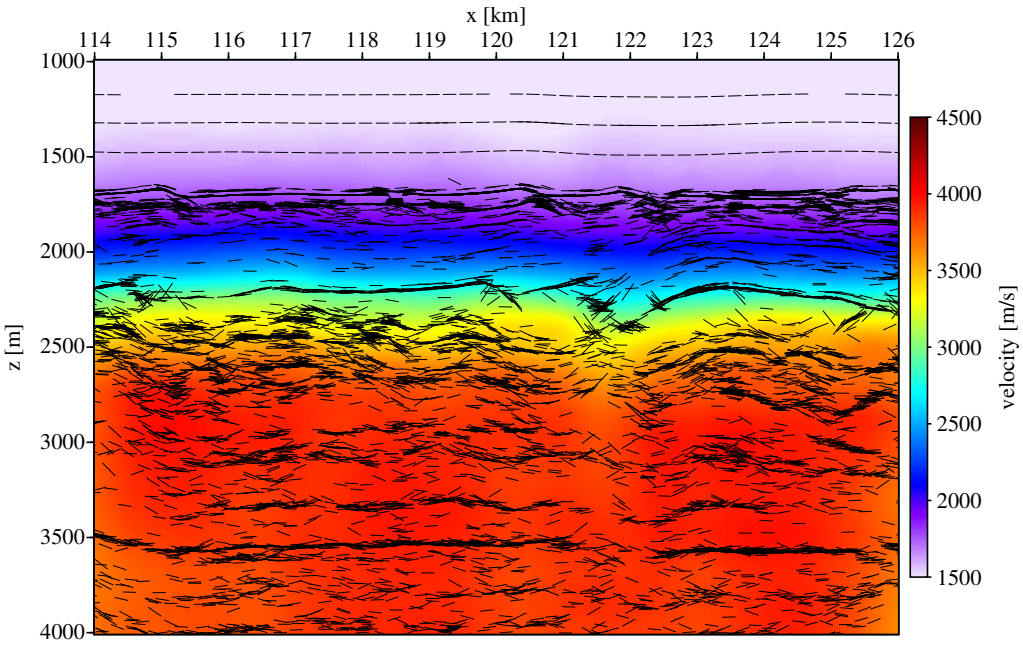


**Figure 3:** The result of stereotomography in the real data case. The velocity model is displayed together with dip bars for each pick. The vertical exaggeration of the section is 1:4.

salt reflection. A further increase of up to 3700 m/s follows and in some parts of the salt layer maximum velocity values of 4000 m/s are observed.
The top of the high-velocity zone seems to be displaced downwards at about $x \approx 121.5$ km. As the distribution of dip bars demonstrates this is a zone of low pick coverage which corresponds to a fault system. The density of dip bars decreases with depth and the velocity model is not very well constrained in this region. For the section between 114 km and 115 km the same situation occurs.
The image as well as selected Common Image Gathers (CIGs) resulting from prestack depth migration are displayed in Fig. 4 and Fig. 5 respectively. The migration results were obtained by a Kirchhoff type algorithm.

Fig. 4 shows a clear image with distinct reflections. The upper sequence of sediments is clearly imaged and the M-reflection is well-defined. The salt layer itself is about 1.4 km thick and the intra-evaporitic sequences can be traced easily since they are continuous over the section, also in the region of the fault structure at about $x \approx 121.5$ km. Beneath this fault the N-reflection is interrupted and downbended and continues on a deeper level on the right side of the section. In addition, as indicated in the velocity model a second fault system is visible at the left boundary of the section. However, both faults are not imaged reliably due to the lack of picks in these regions during velocity model estimation.
The selected CIGs presented in Fig. 5 are equally spaced over the section and a maximum offset of 3 km is shown. The good quality of the image in the upper part is represented by flat gathers throughout the whole section. However, at a depth of about 2000 m negative residual moveout begins to dominate the CIGs. Here, the strong increase in velocity related to the sediment-salt transition could not be described in terms of a smooth velocity model. A further series of events with positive residual moveout can be observed at a depth of approximately 2500 m followed by events which are flattened quite well. The events related to the N-reflection show a slightly positive moveout again. In addition, several linear events in all CIGs appear to interfere with the reflections at large offsets of about 2500 m. These events correspond to refracted waves in the dataset which were not sufficiently suppressed during preprocessing.
Refracted waves can cause problems in stereotomography. The linear moveout of these arrivals leads to high semblance values in the local slant stack and may result in picks. These picks limit correct velocity

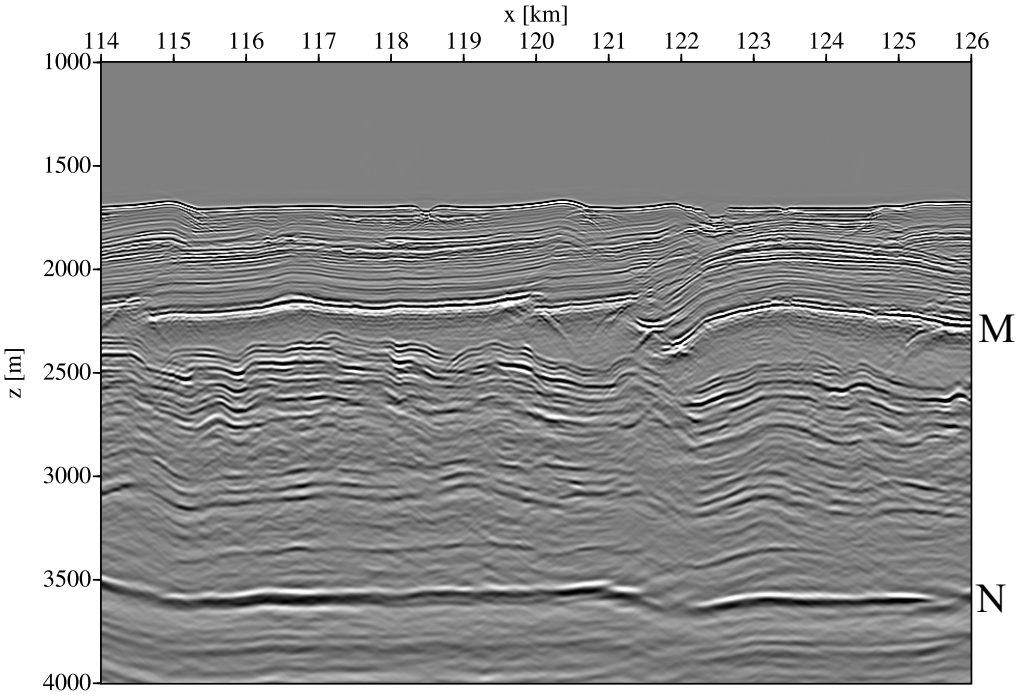


**Figure 4:** The prestack depth migrated image based on the stereotomographic velocity model (data property of *TGS-NOPEC*). The vertical exaggeration of the section is 1:4.

model building as shown by the residual moveout in the CIGs. In spite of the clearly-imaged section the velocity model still needs to be improved and can only be considered as a preliminary result. For successful velocity model estimation, events related to refracted waves have to be removed before stereotomographic inversion.

**NIP-wave tomography results** To process the real data example with NIP-wave tomography a CRS stack was performed in order to determine the required attributes. Afterwards, event consistent parameter smoothing (Hertweck et al., 2005) was applied to obtain 'smoothed' CRS attribute sections where the input data for the inversion were picked. We used an automated picking algorithm to extract the input data. This automated picking tool identifies events in the CRS attribute sections by the semblance criteria. Depending on a pre-defined threshold only the most reliable events are picked. After picking, a quality control was applied to the picked data to remove outliers and unreliable picks (e.g. picks within a fault system). This quality control was based on stacking velocities computed from the picked CRS attributes and mostly followed the practical aspects discussed in Duveneck (2004).

With the extracted and edited picks NIP-wave tomography was performed. An initial B-spline model had to be defined to start the inversion. For the first test we performed the inversion on a grid, and redefined $500$ m $\times$ $500$ m vertical spacing to $100$ m afterwards to achieve a better vertical resolution of the complex salt body. In addition to the input data from the CRS stack, further constraints were introduced to the inversion process. We fixed the top of the velocity model to water velocity and the bottom of the model to an expected velocity of about $3800$ m/s. To further stabilise the inversion, we also defined an initial velocity gradient of $0.45$ s$^{-1}$ for the starting model. All input parameters $\tau, M_{NIP}, p$ and $x$ were weighted equally in the process, meaning we assume that all parameters were determined with the same error.

The result obtained from NIP-wave tomography after ten iterations is visualised in Fig. 6. We clearly see the seafloor at about $1700$ m depth. The velocity increases to $3700$ m/s at a depth of $2200$ m. This corresponds to the M-reflection. Then velocity increases further up to a maximum velocity of $4500$ m/s at

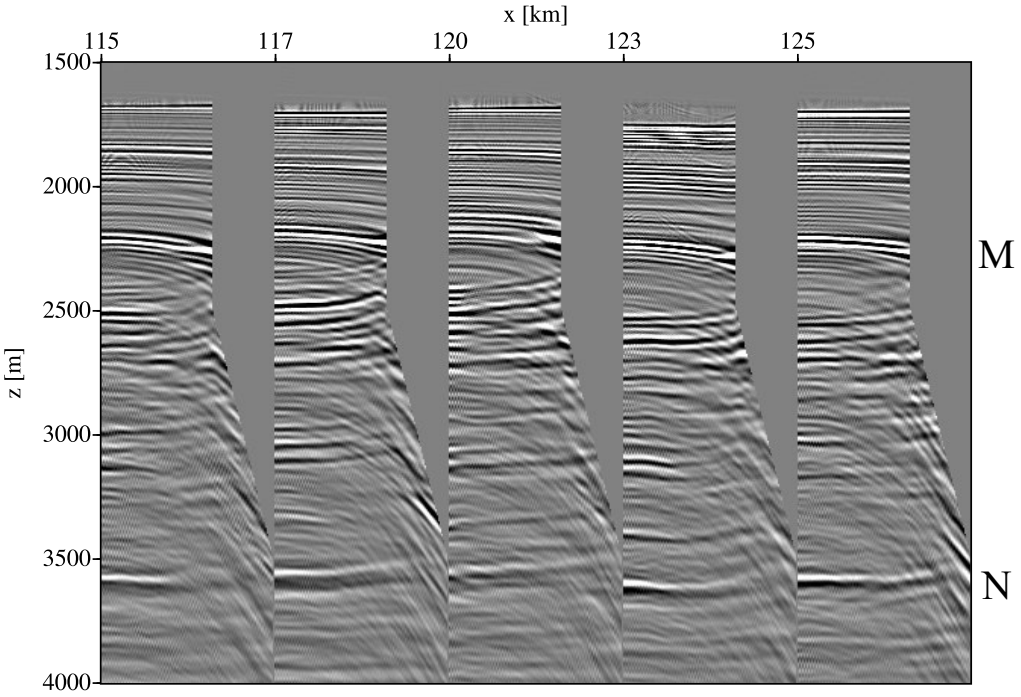


**Figure 5:** Selected Common Image gathers resulting from prestack depth migration based on the stereotomographic velocity model (data property of *TGS-NOPEC*).

a depth of 2600 m. Further in depth, but above the N-reflection the velocity decreases again to the fixed value of 3800 m/s at the bottom of the model.
As in stereotomography the high velocity layer is displaced downwards at approximately $x \approx 121.5$ km. This corresponds to a fault system visible in the CRS stack results. At this position almost no reflections are present and the parameter estimation is not reliable. This argument also holds for the region at position 114 km to 115 km at a depth of about 3500 m. Here it was not possible to determine reliable parameters for the inversion process as well. Due to this a slightly lower velocity of about 3500 m/s is observed in this region which is related to lower values given in the initial velocity model.
The prestack depth migration result is displayed in Fig. 7 as well as selected common image gathers in Fig. 8. The migration results were obtained by a Kirchhoff type algorithm as in the previous section.
In Fig. 7 the image is well focused. As already discussed above we see about 0.5 km of sediments on top of the M-reflection. The same thickness and the same sequences of the salt body are found, but beneath the fault structure at $x \approx 121.5$ km the intra-evaporitic reflections terminate angular against each other. The N-reflection is interrupted and upbended, but continues on the same depth level. In the area of the fault systems, the image lacks of quality as well because the correct migration velocity could not be determined due to poor illumination.
The latter problem is also visible in the CIGs in Fig. 8, where a maximum offset of 3 km is displayed. The gathers located in the fault structures reveal that only the sediment reflections are flattened, but most of the salt reflections have a slight residual moveout. All other CIGs show flattened events for the sediments and the N-reflection. Only some of the intra-evaporitic reflections have a residual moveout. This is probably caused by the input data, because the intra-evaporitic events have lower semblance values then the other events. Therefore, these events are less reliably determined compared to the ones with high semblance values.
We also notice in the CIGs that at large offsets of about 2500 m several events with negative moveout appear, which correspond to refracted arrivals. However, in NIP-wave tomography these events are not considered for velocity estimation since they can not be matched by a hyperbolic traveltime curve.
NIP-wave tomography produces a satisfactory result in terms of flat image gathers in this geologically

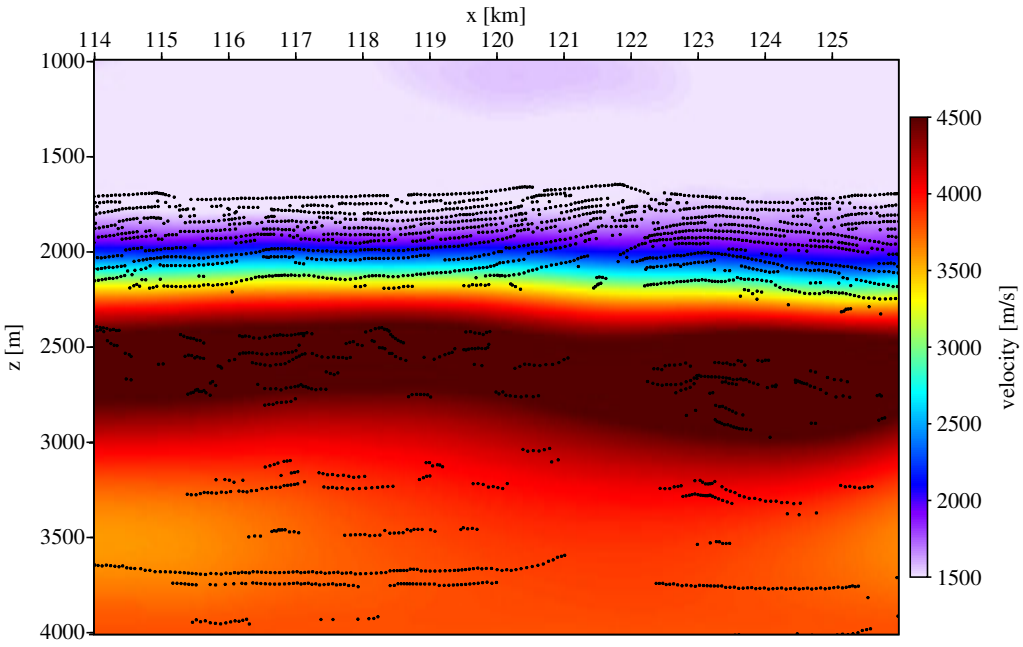


**Figure 6:** The result of NIP-wave tomography in the real data case. The velocity model is displayed together with the input picks. The vertical exaggeration of the section is 1:4.

complex region. Almost all CIGs were flattened and the migration result shows a good quality.

**Comparison** As the real data example demonstrates both tomographic approaches provide a velocity model leading to a clear image in depth. However, despite of the high quality of the imaged sections, major differences occur in the underlying velocity distributions. Whereas the velocity model obtained by NIP-wave tomography leads to a smaller residual move out in the CIGs the stereotomographic velocity distribution results in an image where reflections have a better lateral continuity in regions of low pick coverage. These differences and aspects of application are discussed in the following section.

For prestack stereotomography, discrimination of picks is challenging and important, especially in the presence of refracted waves or noise. Refracted waves lead to high semblance values in the local slant stack panels, since they display a linear moveout. Careful preprocessing and quality control of picks is crucial for the reliable estimation of velocities. In NIP-wave tomography, picking is simplified due to the high signal to noise ratio in the CRS stacked sections. Since only events with high semblance values are selected the inversion process is very stable. NIP-wave tomography is less sensitive to refracted arrivals and requires less preprocessing. However, refracted waves should be removed from the data in any case since they spoil the migrated image. The model obtained by stereotomography has a better lateral resolution since the velocity distribution clearly follows the structure of the M-reflection. In contrast, in NIP-wave tomography smoothing effects are present in areas of strong lateral velocity variation. This is linked to the underlying global approximation of traveltimes. In regions where no information is available the velocity distribution appears to reflect given initial values, whereas in stereotomography no such effect can be observed. In both cases, high velocity contrasts like the M-reflection can be hardly handled by either of the tomographic approaches due to the related smooth velocity model description (see e.g. Fig. 5 and Fig. 8, the associated events in the CIGs are not flattened).
Results obtained by prestack depth migration demonstrate that both velocity models provide similar structures in the imaged sections, Fig. 4 and Fig. 7 respectively. However, the CIGs show that the velocity distribution resulting from NIP-wave tomography seems to better flatten the events in the section. The model obtained by stereotomography still produces some residual moveout. As mentioned above, the presence of noise in form of refracted waves limits a correct velocity model estimation.

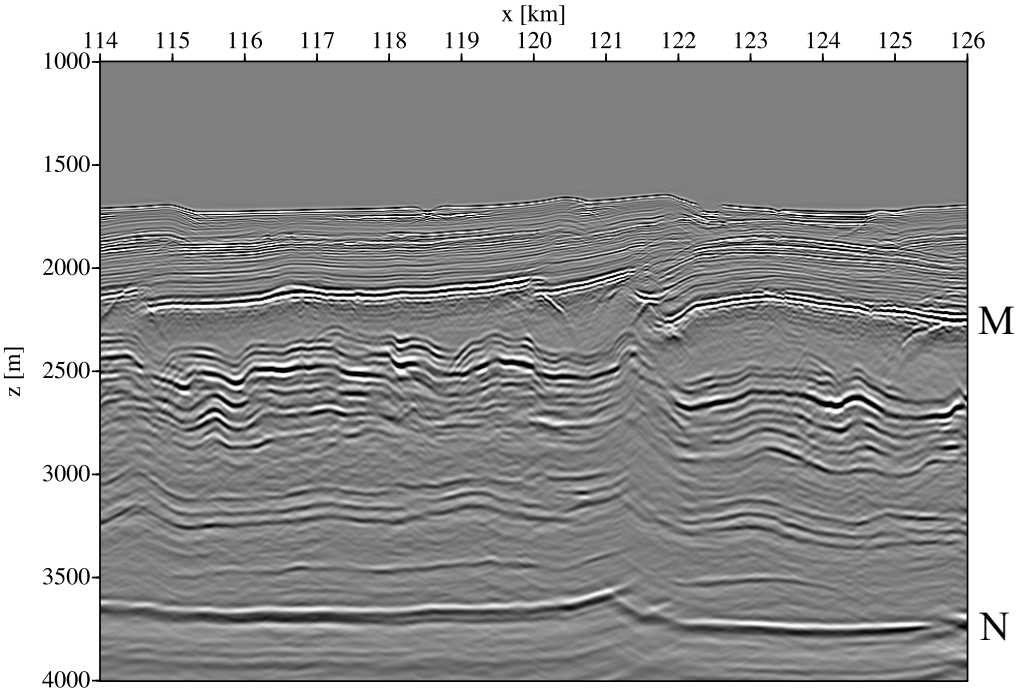


**Figure 7:** The prestack depth migrated image based on the velocity model obtained by NIP-wave tomography (data property of *TGS-NOPEC*). The vertical exaggeration of the section is 1:4.

## CONCLUSIONS

We applied prestack stereotomography and NIP-wave tomography to a synthetic and a real marine dataset in order to compare velocity model estimation by different tomographic approaches in the presence of strong velocity contrasts and lateral variations.

In the case of synthetic data both inversion schemes produced good results. In the constrained areas of the model, the obtained velocity distributions as well as the corresponding migrated sections show hardly any difference. However, due to the smooth description of the model velocity smearing is observed.

In contrast, the real data example reveals other results. NIP-wave tomography provides a good velocity model in terms of flat events in the common image gathers, whereas in stereotomography some residual moveout is observed. The differences in the obtained velocity models are mainly due to the input data determination. For prestack stereotomography, determination of reliable input parameters in the prestack data domain is challenging in the presence of noise or refracted waves. Differences can also be observed regarding the lateral resolution of the velocity distributions. The model obtained by stereotomography seems to follow better the structure of the M-reflection due to the underlying local approximation of traveltimes. Furthermore, in both approaches the characterisation of high velocity contrasts, as due to a salt body, is problematic in terms of the smooth model description of both grid tomographic schemes. Finally, in regions of low pick coverage, velocity estimation is not reliable and differs in both methods as well. The corresponding areas in the migrated image could lead to different geologic interpretations.

To draw final conclusions, this study will be continued. Unwanted events have to be removed from the prestack data to refine velocity model estimation by stereotomography and the impact of the given initial velocity distribution on both inversion schemes will also be tested.

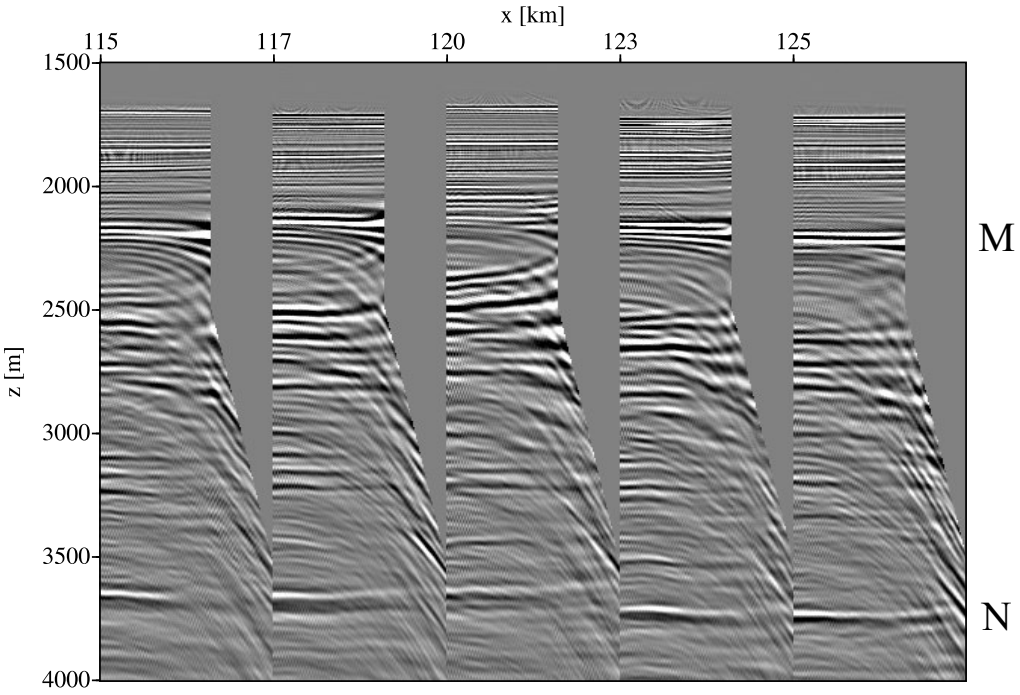


**Figure 8:** Selected Common Image gathers resulting from prestack depth migration based on the velocity model obtained by NIP-wave tomography (data property of *TGS-NOPEC*).

## ACKNOWLEDGEMENTS

This work was supported by the sponsors of the *Wave Inversion Technology (WIT) Consortium*, Karlsruhe, Germany and by the Deutsche Forschungsgemeinschaft through grant *HU 698/14-1*. The real dataset was kindly provided by *TGS-NOPEC*. We especially thank Gilles Lambaré for providing prestack stereotomography and for fruitful discussions and advice. Continuous discussions with the Applied Geophysics Group were always appreciated.

## REFERENCES

Bertoni, C. and Cartwright, J. (2006). Controls on the basinwide architecture of late Miocene (Messinian) evaporites on the Levant margin (Eastern Mediterranean). *Sedimentary Geology*, 188-189:93–114.

Billette, F. and Lambaré, G. (1998). Velocity macro model estimation from seismic reflection data by stereotomography. *Geophys. J. Int.*, 135:671–690.

Billette, F., Le Bégat, S., Podvin, P., and Lambaré, G. (2003). Practical aspects and applications of 2D stereotomography. *Geophysics*, 68:1008–1021.

Duveneck, E. (2004). Velocity model estimation with data-driven wavefront attributes. *Geophysics*, 69:265–274.

Hertweck, T., Mann, J., and Klüver, T. (2005). Event-consistent smoothing in the context of the CRS stack method. *Journal of Seismic Exploration*, 14:197–215.

Hsü, K., Cita, M., and Ryan, W. (1980). *The origin of the Mediterranean Evaporites*. U.S. Govt. Printing Office, Washington D.C.

Hubral, P. and Krey, T. (1980). *Interval velocities from seismic reflection traveltime measurements*. Soc. Expl. Geophys., Tulsa.

Lambaré, G., Alerini, M., Baina, R., and Podvin, P. (2004a). Stereotomography: a semi-automatic approach for velocity macromodel estimation. *Geophysical Prospecting*, 52:671–681.

Lambaré, G., Alerini, M., and Podivn, P. (2004b). Stereotomographic picking in pratice. *DIG annual report*, 4:9–44.

MacKay, S. and Abma, R. (1992). Imaging and velocity estimation with depth-focussing analysis. *Geophysics*, 57:1608–1622.

Mann, J. (2002). *Extensions and Applications of the Common-Reflection-Surface Stack Method*. Ph. D. thesis, University of Karlsruhe.

Netzeband, G., Gohl, K., Hübscher, C., Ben-Avraham, Z., Dehghani, A., Gajewski, D., and Liersch, P. (2006a). The Levantine Basin - crustal structure and origin. *Tectonophysics*, 418:178–188.

Netzeband, G., Hübscher, C., and Gajewski, D. (2006b). The structural evolution of the Messinian Evaporites in the Levantine Basin. *Marine Geology*, 230:249–273.

Paige, C. C. and Saunders, M. A. (1982). LSQR: An algorithm for sparse linear equations and sparse least squares. *ACM Trans. Math. Softw.*, 8:43–71.